Applying the Virtual Fields Method to measure during milling the through-thickness residual stress distribution in aluminum-alloy sheet material

Théo Jovani, Benoît Blaysat, Hélène Chanal, Michel Grédiac

Applying the Virtual Fields Method to measure during milling the through-thickness residual stress distribution in aluminum-alloy sheet material

Théo Jovani[1], Benoît Blaysat[1], Hélène Chanal[1] and Michel Grédiac[1*]

Institut Pascal, UMR 6602, Université Clermont-Auvergne, CNRS, SIGMA Clermont, 20 avenue Blaise Pascal,TSA 62006, Aubière CEDEX, 63178, France.

*Corresponding author(s). E-mail(s): michel.grediac@uca.fr;
Contributing authors: theo.jovani@sigma-clermont.fr;
benoit.blaysat@uca.fr; helene.chanal@sigma-clermont.fr;

Abstract

Background: Residual stresses often cause distortion to occur when machining slender workpieces like those used in aeronautics. This distortion is undesirable and may even cause the workpiece to be scrapped. Identifying these residual stresses during machining is therefore crucial to limit their effect on the final geometry of the part.

Objective: The aim of this work is to identify the through-thickness residual stress distribution by processing displacement/strain fields measured on the workpiece during machining.

Methods: Digital Image Correlation is employed to measure, between successive milling passes, the displacement and strain fields on the lateral surface of the workpiece. These fields are then processed with the Virtual Fields Method to identify the through-thickness residual stress distribution. Compared to previous studies on this topic, no assumption is made concerning the real through-thickness displacement field.

Results: Simulations performed with synthetic data provided by a finite element model show the feasibility of this approach and quantifies its robustness when displacements are affected by measurement noise. Results obtained with this approach in a real case are then compared with their counterparts obtained with another identification technique, which assumes that the workpiece behaves as a beam.
Conclusion: This study shows that it is possible to measure the through-thickness distribution of residual stress in slender workpieces during machining by using a classic subset-based DIC software and the Virtual Fields Method to process the displacement/strain maps. This opens the way for future developments aimed for instance at updating in live machining sequences in order to obtain machined parts immune from distortions caused by residual stresses.

Keywords: Digital Image Correlation, Displacement field, Machining, Residual stress, Virtual Fields Method

1 Introduction

Full-field measurements techniques such as Digital Image Correlation (DIC) have widely disseminated among the experimental mechanics community in the recent past Grédiac and Hild (2012). Indeed, such techniques enable the users to measure displacement or strain distributions over the external surface of tested specimens, if not in their bulk Sutton et al (2009). Such fields are useful to observe localized phenomena that occur when materials are loaded or, within the framework of Material Testing 2.0 Pierron and Grédiac (2021), to identify parameters governing constitutive equations by using numerical strategies suitable for testing configurations giving rise to heterogeneous strain fields. Comparatively, manufacturing issues seem to have been intensively addressed with this type of tool only in the case of metal forming, for which forming limit curves can be deduced from this type of measurement, Pottier et al (2012); Mishra and Thuillier (2014); Schwindt et al (2015); Billur (2020) for instance, or for the characterization of welded joints, Louëdec et al (2013); Texier et al (2016); Milosevic et al (2021); Corigliano et al (2021) for instance.

Indeed, the use of DIC is only seldom described as a measuring tool directly placed in machining centers or other similar machine tools. In Harzallah et al (2018), DIC and infrared thermography were used simultaneously to investigate orthogonal cutting. In Rebergue et al (2018, 2022), the warping of a workpiece caused by residual stresses was measured by DIC during milling, the underlying objective and ultimate goal being to update in live machining sequences to counterbalance the negative impact of these stresses on the final geometry of machined parts. Another benefit of measuring such through-thickness residual stress distributions is to perform finite element simulations in which the load applied to the workpiece is this residual stress distribution measured during milling. This enables the users to predict the warping of the workpieces during machining, and thus to adjust and adapt the machining sequence accordingly. As a general remark, several methods have been presented in the literature to estimate residual stress distributions, see the survey presented in Cheng and Finnie (2007). All these techniques share the same feature: the residual stress is released, and the resulting change of geometry is measured. As a consequence, these methods are destructive. They mainly differ in the way the residual stress is released. The most popular methods rely on successive layer removals from plate or beam specimens Treuting and Read (1951); Hospers and Vogelesang (1975); Jiang et al (2011); Dreier and Denkena (2014), on slitting Cheng and Finnie (2007); Salehi et al (2020), slotting Olson et al (2022) or cracking Prime and Hill (2002). The hole drilling method is probably the least destructive one Gao and Shang (2009); Baldi (2014, 2019); Razumovskii and Usov (2021), because the diameter of the hole can potentially be small. Even a standard is available for this technique ASTM (2021). Given the context of the present study, which is aimed to estimate residual stress distributions through the thickness of workpieces during milling

to adjust and adapt the machining sequence, we only focus here on the layer removal technique.

As explained above, the change in geometry must be measured to estimate the residual stress which is released. The classic route is to employ strain gages or displacement sensors. The use of such sensors is well established and well documented. They are however limited to local measurements. DIC has been used in some studies to measure residual stress distributions with the hole drilling method Gao and Shang (2009); Baldi (2014, 2019) or with slitting Salehi et al (2020), the benefit being to provide full-field measurements, but estimating such stress distributions during manufacturing is quite challenging because this is a harsh environment. Indeed, vibrations often blur the images and cutting chips locally hide the part or cause light reflection to occur. In Rebergue et al (2018, 2022), the objective was mainly to adapt DIC so that it could be used in this type of environment. In these last two references, the residual stress distribution was however not directly deduced from the displacement fields measurement during milling. After Treuting and Read (1951), Hospers and Vogelesang (1975) proposed to deduce, under mild assumptions, the through-thickness residual stress distribution in elongated parts by measuring their curvature between consecutive layer removals. This curvature was not measured by using a full-field measuring technique. Indeed, it was deduced from the coordinates of three different points. These coordinates were measured by means of a microscope which was attached to a pair of micrometer slides. The workpiece had however to be unmounted after each pass to perform this measurement. The procedures presented in Hospers and Vogelesang (1975); Rebergue et al (2018, 2022) were recently combined in Jovani et al (2022), where the through-thickness residual stress profile was measured from curvature deduced from DIC measurements. In this last paper however, the

theoretical procedure proposed in Hospers and Vogelesang (1975) was not questioned. The spread of full-field measurement techniques has however led their users to propose identification procedures in which the wealth of data provided by such techniques is accounted for. For instance, some papers describing the use of the Virtual Fields Method (VFM) to measure the load applied to tested specimens are available in the literature, full-field displacement or strain fields being measured with a suitable full-field measurement technique. This identification technique was used in Pierron et al (2011) to measure the force applied on a specimen during an impact test, in Berry et al (2014); Berry and Olivier (2016); O'Donoughue et al (2019); Kaufmann et al (2019); Olufsen et al (2022) to measure the dynamic loading applied on vibrating plates, in Kaufmann et al (2019) to estimate the full-field surface pressure applied by an impinging air jet to a bent plate, and in Kaufmann et al (2022) to measure surface pressures on flat plates impacted by blast waves.

In this context, the objective of this paper is to use the VFM in order to measure the stress distribution through the thickness of a slender part under milling. The displacement and strain fields are estimated by DIC on the lateral surface of the part, the camera being directly embedded in the machine tool.

The paper is organized as follows. The basics of the VFM are recalled in Section 2. It is then explained in Section 3 how to use this method to measure the through-thickness residual stress distribution which occurs within a workpiece during machining. In Section 4, the procedure is first applied on synthetic data provided by finite element simulations. We finally discuss in Section 5 the advantage of this approach by processing experimental data. These results are compared with those obtained in Jovani et al (2022), in which the procedure proposed in Hospers and Vogelesang (1975) is employed.

2 The Virtual Fields Method: a brief reminder

The Virtual Fields Method is an identification technique which was introduced to process displacement or strain fields measured for instance by DIC Sutton et al (2009) or by other full-field measurement techniques such as the grid method Grédiac et al (2016) or interferometric moiré Cao et al (2020). It has been mainly proposed to measure parameters governing various types of constitutive equations Pierron and Grédiac (2012). Compared to the classic finite element model updating technique, the main advantage of the VFM is its much lower computational cost while keeping a good robustness when noisy data are processed Zhang et al (2017); Martins et al (2018). This probably explains why this technique has been used in a wide range of applications in the recent years within the framework of Material Testing 2.0 Pierron and Grédiac (2021).

The VFM relies on the Principle of Virtual Work (PVW), which is nothing but the weak form of equilibrium Dym and Shames (1973). This principle is often used to introduce the finite element method but it has been shown in Grédiac (1989) that it could be advantageously used for identifying the parameters governing constitutive equations from heterogeneous strain fields, assuming the latter are measured on the surface of the tested specimen.

The PVW is obtained by considering first the local equilibrium equation. This equilibrium reads as follows is statics

$$\underline{\mathrm{div}}(\underline{\underline{\sigma}}) + \underline{f} = \underline{0}, \tag{1}$$

where $\underline{f}$ is the volume force applied at any point of the solid and $\underline{\underline{\sigma}}$ the stress tensor. This equation, which is satisfied at any point of a solid, is then multiplied by any vector denoted by $\underline{u}^*$ belonging to the $\mathcal{H}^1(\Omega)$ Sobolev space. The first term is then integrated over the solid or any portion of it denoted by Ω.

$\underline{u}^*$ is referred to as a *test function* in mathematics but this vector is generally considered as a virtual displacement in continuum mechanics, which leads the quantity obtained by integration to be a virtual work. Thus

$$\int_\Omega \underline{\mathrm{div}}(\underline{\underline{\sigma}}).\underline{u}^* \mathrm{d}\Omega + \int_\Omega \underline{f}.\underline{u}^* \mathrm{d}\Omega = 0, \ \forall \underline{u}^* \in \mathcal{H}^1(\Omega), \tag{2}$$

where symbol "." represents the dot product of two vectors. One of the features of the PVW is that it is rigorously satisfied for an infinite number of virtual fields $\underline{u}^*$ Dym and Shames (1973).

After integrating by parts the first integral and reordering the different quantities, we get

$$W_{int}^* + W_{ext}^* = 0, \ \forall \underline{u}^* \in \mathcal{H}^1(\Omega). \tag{3}$$

W_{int}^* is the internal virtual work and W_{ext}^* the external virtual work. The latter is obtained by integrating the product of any traction acting over the boundary $\partial\Omega$ and $\underline{u}^*$, by multiplying any isolated force by the value of $\underline{u}^*$ at the point where this force is applied, and by multiplying any isolated moment by the local virtual rotation induced by the virtual displacement field. The internal virtual work W_{int}^* is the opposite of the doubled contracted product between the stress tensor $\underline{\underline{\sigma}}$ and the virtual strain tensor $\underline{\underline{\epsilon}}^*$ over Ω. Thus

$$W_{int}^* = -\int_\Omega \underline{\underline{\sigma}} : \underline{\underline{\epsilon}}^* \mathrm{d}\Omega \tag{4}$$

where symbol ":" represents the doubly contracted product of two second-rank tensors.

With the VFM, the first idea is to express the stress field as a function of the strain field by using the constitutive equations of the material. Assuming here that these constitutive equations and that the material parameters are known, W_{int}^* is completely determined for any virtual displacement if the strain field is

measured throughout Ω. In practice, tested specimens are generally thin along one dimension, thus measuring the strain field over one of the external surface is sufficient, the though-thickness distribution being deduced by assuming it is uniform in case of in-plane problem, or linear in the case of bent plates with the classic Love-Kirchhoff assumption. With the initial version of the VFM, the parameters governing the constitutive equations are the unknowns to be determined and the applied loading is measured, so W^*_{ext} is completely determined for any virtual field (VF). The PVW is then written with different VFs chosen by the user and the parameters are deduced from a set of equations, each of them being obtained for a new VF. In the case of linear elasticity, at least as many independent VFs as unknowns shall be used. This leads to a linear system which provides the unknown parameters after inversion Pierron and Grédiac (2012). In the present case of load characterization, we assume that the constitutive equations of the material as well as the set of parameters governing these equations are known, and that the load is unknown. We will show hereafter that the problem at hand reduces to determining a maximum number of unknowns, which is equal to one per removed layer. Hence, since the PVW will be written after each layer removal, only one VF per removed layer will be sufficient to identify the whole set of unknowns.

3 Applying the Virtual Fields Method to identify the residual stress distribution from successive milling passes

3.1 Introduction

We consider now the case of residual stress characterization from a displacement field measured by DIC on the lateral surface $(O, \underline{e}_x, \underline{e}_y)$ of a parallelepiped

workpiece, as illustrated in the schematic view shown in Figure 1a. As proposed in Hospers and Vogelesang (1975), the problem is assumed to be invariant along the $\underline{e}_z$ direction. Consequently, the VFM is reduced to its 2D formulation. It is therefore only applied to the surface where the displacement field is measured. The geometry of the machined workpiece is known. This is a short beam of length $L = 400$ [mm] and thickness $h = 100$ [mm], which will be considered as extracted from a beam, which is infinite along the x-direction only, the problem being assumed to be invariant along the z-direction. This infinite plate has the same initial thickness as the raw part just before the first layer removal. This latter assumption will turn out to be useful when discussing the external load applied to the workpiece, see Section 3.4 below. The response of the material is assumed to be linear elastic. Its Young's modulus and Poisson's ratio are known.

The goal here is to determine the residual stress distribution through the thickness of the initial raw part. This residual stress tensor is denoted by $\underline{\underline{\sigma}}_r$. For that purpose, the VFM is applied on domain Ω obtained after the removal of layer $\#i$ and before removal of layer $\#(i+1)$, which means that no force exerted on the workpiece by the mill is considered in W^*_{ext}. The workpiece is suspended between two clamps, so no external force acting between them on the bottom surface of the workpiece between the supports is considered either. Ω is defined by $\Omega = \{(x, y) \in [0, L] \times [0, h - e]\}$, where e is the thickness of the portion of the part removed by milling. It corresponds to the red box in Figure 1a. The same assumption as in Hospers and Vogelesang (1975) is considered here about the number of unknown components to be determined in $\underline{\underline{\sigma}}_r$. Consequently, only the xx-component is non-null, and this quantity remains constant along the x-direction within the whole workpiece. Hence $\underline{\underline{\sigma}}_r$ is a function of y only. Thus,

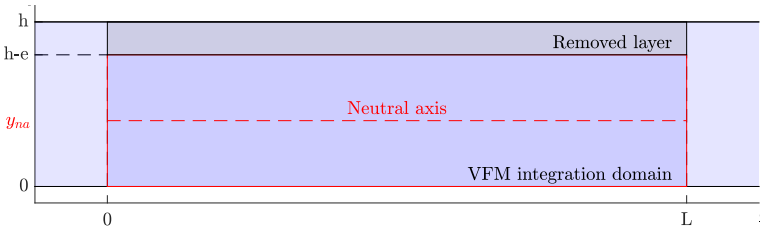

(a) Domain where the VFM is applied

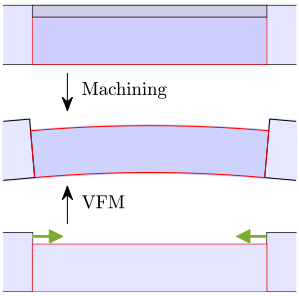

(b) Illustration of the VFM strategy.

Fig. 1: Domain geometry (a) and illustration of the case for the VFM (b). Details of (b): Top: raw workpiece before machining. Middle: workpiece bent after the elastic release of the residual stress due to a layer removal. Bottom: initial geometry workpiece, in which the effect of the machined layer to the top left part of the workpiece is modeled by tractions acting on the vertical sections, which correspond to the initial residual stress.

$$\underline{\underline{\sigma}}_r = \sigma_r(y)\ \underline{e}_x \otimes \underline{e}_x, \tag{5}$$

where symbol "$\otimes$" denotes the outer product of two vectors. In Figure 1b, the loading that the layer removed at the top applies to Ω therefore consists of a traction vector of direction $\underline{e}_x$, applied on a surface of normal $\underline{e}_x$. Applying the VFM to Ω allows the determination of theses forces that vanish during machining, as illustrated in Figure 1b.

The objective now is to write in detail the two quantities W^*_{int} and W^*_{ext} involved in the PVW given in Equation 3 but to do so, we first need to define a virtual field $\underline{u}^*$ suited to the problem at hand. This is the aim of the following section.

3.2 Choice of a suitable virtual field $\underline{u}^*$

In Refs. Hospers and Vogelesang (1975); Jovani et al (2022), it is assumed that the machined workpiece is thin. The classic kinematic assumption linking curvature and through-thickness displacement is therefore introduced in these references. More precisely, the horizontal displacement and normal strain at any point of the cross-section are considered to linearly depend on the local curvature and on the distance to the neutral axis. With the present approach however, the entire real displacement and strain fields are measured over the lateral surface of the workpiece, so no model is necessary to describe these real fields. On the other hand, a virtual displacement field must be defined and we found it relevant to use here a virtual displacement field, which satisfies the classic assumption recalled above. The reason is mainly that u_x and ϵ_{xx} are globally expected to feature a change of sign between the top and bottom of the machined part. As shown in Equation 4, the integral defining W^*_{int} can be regarded as a weighted sum of the real strain measured through the thickness of the workpiece, the value of the weight being given by the virtual strain. Thus having both a real and a virtual strain distributions featuring both the same sign over the main part of the workpiece ensures the integrand involved in Equation 4 to have the same sign over Ω. This property of non-changing sign over Ω is expected to cause the integral, thus the identified residual stress, to be less sensitive to noisy strain data than if the sign fluctuates over Ω, and this property is achieved to a large extent if the virtual displacement field

satisfies the kinematic assumption recalled above. Another constraint is that the virtual displacement of the neutral axis shall be null at $x = 0$ and $x = L$ in order to nullify the contribution to W^*_{ext} of both the forces applied by the clamps to the workpiece and the reaction forces at the support. The reason is that these forces are not measured and thus remain unknown.

It is worth emphasizing that contrary to the identification procedure discussed in Refs. Hospers and Vogelesang (1975); Jovani et al (2022), no assumption is made here concerning the *real* through-thickness displacement, the latter being directly measured. The fact that the *virtual* displacement is chosen to satisfy here the classic kinematic assumption does not induce any approximation, Equation 3 above being *exactly* valid in this case. This is no longer true if the *real* displacement field follows this assumption: an approximation is made in this case and Equation 3 above is then only *approximately* valid. It also means that thicker parts or more complex geometries than that studied in the present paper can potentially be investigated with the present approach, as long as the displacement field measured by DIC on the lateral surface is representative of the displacement through the width of the part.

As a conclusion, the following general form for $\underline{u}^*$ is chosen here:

$$\forall (x,y) \in \Omega, \quad \underline{u}^*(x,y) = -(y - y_{na}) \frac{dv^*_{na}}{dx}(x) \underline{e}_x + v^*_{na}(x) \underline{e}_y, \tag{6}$$

where v^*_{na} is the virtual deflection of the neutral axis of Ω. This neutral axis is defined by $y = y_{na}$, see Figure 1a.

As explained above, the residual stress field is assumed to be uniaxial along the x-direction but this assumption is potentially questionable near the left- and right-hand sides of the workpiece. The reason is that we have here free boundaries, and that tractions are always rigorously null along such boundaries. It can therefore reasonably be assumed thanks to the Saint-Venant's

principle that the stress field is three-dimensional within these last two zones, and one dimensional only away from them, thus at the center of the work-piece. With the PVW, we can easily get rid of the contribution of the left- and right-hand sides by defining virtual displacement fields which are rigid-body like in these zones, virtual strains being not null only at the center. Such virtual fields can easily be obtained by defining them piecewisely, over three contiguous domains denoted by $\mathcal{D}_1$, $\mathcal{D}_2$ and $\mathcal{D}_3$ (see Figure 2), both the function defining the virtual displacement of the neutral axis and its first derivatives being continuous between neighboring domains. We consider for this the virtual deflection v^*_{na} plotted in Figure 2.

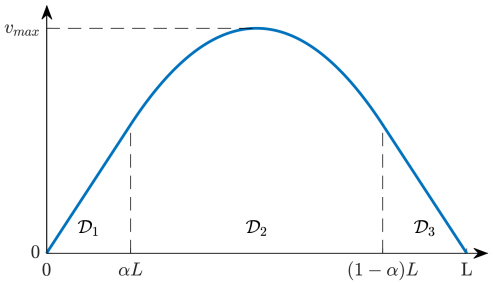

Fig. 2: Piecewise virtual deflection of the neutral axis, $\alpha \in [0\ 0.5]$.

This virtual deflection is such that a virtual rigid-body motion occurs over $\mathcal{D}_1$ (thus for $x \in [0\ \alpha L]$) and $\mathcal{D}_3$ ($x \in [(1-\alpha)L\ L]$). The virtual strains will therefore be null in $\mathcal{D}_1$ and $\mathcal{D}_3$, thus cancelling out the contribution to the internal virtual work W^*_{int} of the potentially tridimensional stress field in these zones. A quadratic function completes the definition of the virtual field over

$\mathcal{D}_2$ by C^1 continuity. Thus

$$\begin{cases} \mathcal{D}_1 : x \in [0\ \alpha L] & v^*_{na}(x) = (1-2\alpha)\, x \\ \mathcal{D}_2 : x \in [\alpha L\ (1-\alpha)L] & v^*_{na}(x) = \left((1-2\alpha)\alpha - \left(\frac{x}{L} - \alpha\right)\left(\frac{x}{L} - (\alpha-1)\right)\right) L\ , \\ \mathcal{D}_3 : x \in [(1-\alpha)L\ L] & v^*_{na}(x) = (1-2\alpha)\,(L-x) \end{cases} \tag{7}$$

and

$$\begin{cases} \mathcal{D}_1 : x \in [0\ \alpha L] & \dfrac{dv^*_{na}}{dx}(x) = 1-2\alpha \\ \mathcal{D}_2 : x \in [\alpha L\ (1-\alpha)L] & \dfrac{dv^*_{na}}{dx}(x) = 1-2\frac{x}{L}\ . \\ \mathcal{D}_3 : x \in [(1-\alpha)L\ L] & \dfrac{dv^*_{na}}{dx}(x) = 2\alpha-1 \end{cases} \tag{8}$$

The virtual strain components can be deduced by derivation, which gives $\varepsilon^*_{yy} = \varepsilon^*_{xy} = 0$. Since we have by definition $\varepsilon^*_{xx}(x,y) = -(y-y_{na})\dfrac{d^2 v^*_{na}}{dx^2}(x)$, $\varepsilon^*_{xx}(x,y)$ is equal to

$$\varepsilon^*_{xx}(x,y) = \begin{cases} 2\left(\dfrac{y-y_{na}}{L}\right) & \forall x \in \mathcal{D}_2 \\ 0 & \forall x \in \mathcal{D}_1 \cup \mathcal{D}_3 \end{cases}. \tag{9}$$

3.3 Determination of the internal virtual work W^*_{int}

Since the only non-null virtual strain component over $\mathcal{D}_2$ is ε^*_{xx}, W^*_{int} reduces to

$$W^*_{int} = -\int_{y=0}^{h-e}\int_{x=\alpha L}^{(1-\alpha)L} 2\frac{y-y_{na}}{L}\sigma_{xx}(x,y)\mathrm{d}x\mathrm{d}y. \tag{10}$$

The aspect ratio of the part being small, σ_{xx} is then substituted as in Hospers and Vogelesang (1975) by $\dfrac{E}{1-\nu^2}\varepsilon_{xx}$ by using the Hooke's law. This finally gives

$$W_{int}^{*} = -\frac{2E}{(1-\nu^2)\,L}\int_{y=0}^{h-e}\int_{x=\alpha L}^{(1-\alpha)L}(y-y_{na})\varepsilon_{xx}(x,y)\mathrm{d}x\mathrm{d}y. \qquad (11)$$

In this quantity, ε_{xx} is known since it is measured by DIC over the lateral surface of the specimen. α is chosen by the user (the influence of this parameter on the quality of the results is discussed in Section 4.6 below), thus all the ingredients involved in W_{int}^{*} are known. A consequence is that W_{int}^{*} is perfectly determined.

3.4 Determination of the external virtual work W_{ext}^{*}

The external work is split into four quantities by considering separately the four lines defining the border of the domain. Thus

$$W_{ext}^{*} = W_{ext,L}^{*} + W_{ext,R}^{*} + W_{ext,T}^{*} + W_{ext,B}^{*}, \qquad (12)$$

with

$$\begin{cases} W_{ext,L}^{*} = \int_{y=0}^{h-e}(\underline{\underline{\sigma}}(0,y)(-\underline{e}_x)).\underline{u}^{*}(0,y)\mathrm{d}y \\ W_{ext,R}^{*} = \int_{y=0}^{h-e}(\underline{\underline{\sigma}}(L,y)\underline{e}_x).\underline{u}^{*}(L,y)\mathrm{d}y \\ W_{ext,B}^{*} = \int_{x=0}^{L}(\underline{\underline{\sigma}}(x,0)(-\underline{e}_y)).\underline{u}^{*}(x,0)\mathrm{d}y \\ W_{ext,T}^{*} = \int_{x=0}^{L}(\underline{\underline{\sigma}}(x,h-e)\underline{e}_y).\underline{u}^{*}(x,h-e)\mathrm{d}y \end{cases}. \qquad (13)$$

These four quantities can be determined in turn:

- $W_{ext,L}^{*}$: The equilibrium of the cross section of the initial part defined by $(x=0, y\in[0,h])$ can be written by considering separately the contribution to the virtual work of the left-hand side of Ω (defined by $(x=0, y\in[0,h-e])$) and the contribution to the virtual work of the left-hand side of the removed layer (thus $(x=0, y\in[h-e,h])$). We merely write that $\forall\underline{u}^{*}\in\mathcal{H}^{1}(\Omega)$, the virtual work of the traction vector calculated over the whole

cross section of the initial part is null. Then, this quantity is split into two different parts, which are the contributions to the virtual work of each of these two surfaces, namely $(x = 0, y \in [0, h - e])$ on the one hand and $(x = 0, y \in [h-e, h])$ on the other hand. Thus the contribution to the virtual work of the traction vector over the zone defined by $(x = 0, y \in [0, h - e])$ is balanced by the contribution to the virtual work of the traction vector over the zone defined by $(x = 0, y \in [h - e, h])$. This reads as follows:

$$\int_{y=0}^{h-e} (\underline{\underline{\sigma}}(0,y)(-\underline{e}_x)).\underline{u}^*(0,y)\mathrm{d}y + \int_{y=h-e}^{h} (\sigma_r(y)\, \underline{e}_x \otimes \underline{e}_x)\underline{e}_x.\underline{u}^*(0,y)\mathrm{d}y = 0 \; \forall \underline{u}^* \in \mathcal{H}^1(\Omega). \tag{14}$$

By introducing the virtual field defined above, we get

$$W^*_{ext,L} = (1 - 2\alpha) \int_{y=h-e}^{h} \sigma_r(y)(y - y_{na})\mathrm{d}y. \tag{15}$$

- $W^*_{ext,R}$: A similar equation can be written to determine the external virtual work of the traction vector over the right-hand side of Ω:

$$W^*_{ext,R} = (1 - 2\alpha) \int_{y=h-e}^{h} \sigma_r(y)(y - y_{na})\mathrm{d}y. \tag{16}$$

- $W^*_{ext,B}$: The bottom border defined by $(x \in [0, L], y = 0)$ is not subjected to any load. As a consequence, $W^*_{ext,B} = 0$.
- $W^*_{ext,T}$: As depicted in Figure 1b and as discussed above, the removed layer does not apply any load to Ω over its upper surface, *i.e.* the surface defined by $(x \in [0, L],\ y = h - e)$. Thus $W^*_{ext,T} = 0$.

By substituting in Equations 12 and 13 the four quantities defined above, W^*_{ext} eventually reduces to the following expression:

$$W^*_{ext} = 2(1-2\alpha)\int_{y=h-e}^{h} \sigma_r(y)(y-y_{na})\mathrm{d}y. \tag{17}$$

3.5 Determination of the residual stress distribution in the raw part

The objective now is to deduce the residual stress distribution $\sigma_r(y)$ in the raw part $\forall y \in [0,h]$. The expressions of W^*_{int} and W^*_{ext} obtained above are used to reach this goal. The PVW is then applied each time a layer is removed.

3.5.1 Weighted integrated form of the residual stress

Substituting first in Equation 3 the expressions of W^*_{int} and W^*_{ext} defined in Equations 11 and 17 leads to:

$$2(1-2\alpha)\int_{y=h-e}^{h} \sigma_r(y)(y-y_{na})\mathrm{d}y - \frac{2E}{(1-\nu^2)\,L}\int_{y=0}^{h-e}\int_{x=\alpha L}^{(1-\alpha)L}(y-y_{na})\varepsilon_{xx}(x,y)\mathrm{d}x\mathrm{d}y = 0 \tag{18}$$

The idea is to write this equation layerwise, the displacement/strain fields being measured by DIC at the end of each pass, without removing the workpiece from its support. These maps are obtained by considering that the reference state is the raw part, and the deformed state the machined part after step $\#i$. For the sake of simplicity, we consider here the case for which the layers removed at each pass have the same thickness denoted by Δe. Hence, the total thickness removed at step $\#i$ being denoted by $e^{(i)}, i \cdots n$, where n is the total number of layers that are finally removed, we have $e^{(i)} = i \times \Delta e$.

Denoting by $\varepsilon^{(i)}_{xx}$ the strain map obtained with DIC at each step $\#i$, writing n times Equation 18 leads to a system of n equations. Each of these equations reads as follows:

$$(1-2\alpha)\int_{y=h-e^{(i)}}^{h}\sigma_r(y)(y-y_{na})\mathrm{d}y-\frac{E}{(1-\nu^2)\,L}\int_{y=0}^{h-e^{(i)}}\int_{x=\alpha L}^{(1-\alpha)L}(y-y_{na})\varepsilon_{xx}^{(i)}(x,y)\mathrm{d}x\mathrm{d}y=0, \tag{19}$$

For each increment, the integral form of the residual stress, denoted by $\Sigma_r^{(i)}$ is obtained as follows:

$$\Sigma_r^{(i)} = \int_{y=h-e^{(i)}}^{h}\sigma_r(y)(y-y_{na})\mathrm{d}y \tag{20}$$

$$= \frac{E}{(1-\nu^2)\,(1-2\alpha)L}\int_{y=0}^{h-e^{(i)}}\int_{x=\alpha L}^{(1-\alpha)L}\left(y-\frac{h-e^{(i)}}{2}\right)\varepsilon_{xx}^{(i)}(x,y)\mathrm{d}x\mathrm{d}y, \forall i\in\{1,...,n\} \tag{21}$$

Once the quantities $(\Sigma_r^{(i)})_{1\leq i\leq n}$ are known, two procedures are proposed to determine the distribution of the initial residual stress within the raw workpiece. With the first procedure, the average residual stress is provided stepwise, so the output of the identification procedure is a set of n values of residual stress. With the second procedure, we consider that the residual stress distribution is modeled by a polynomial function, and the coefficients defining the polynomial are the unknowns returned by the identification procedure. These two procedures are presented in turn in the following two sections.

3.5.2 Procedure #1: Retrieving the average residual stress in each layer

The first approach is similar to the one proposed in Hospers and Vogelesang (1975). It aims to retrieve the average residual stress in each layer. This quantity is denoted by $\langle\sigma_r^{(i)}\rangle$. It is defined as follows:

$$\langle \sigma_r^{(i)} \rangle = \frac{1}{e^{(i)} - e^{(i-1)}} \int_{y=h-e^{(i)}}^{h-e^{(i-1)}} \sigma_r(y) \mathrm{d}y = \frac{1}{\Delta e} \int_{y=h-i\Delta e}^{h-(i-1)\Delta e} \sigma_r(y) \mathrm{d}y \tag{22}$$

The weighted integral form $\Sigma_r^{(i+1)}$ is rewritten as follows:

$$\Sigma_r^{(i+1)} = \int_{y=h-e^{(i+1)}}^{h} \sigma_r(y) \left(y - \frac{h - e^{(i+1)}}{2} \right) \mathrm{d}y \tag{23}$$

$$\approx \Sigma_r^{(i)} + \frac{\Delta e^2}{2} \sum_{j=1}^{i-1} \langle \sigma_r^{(j)} \rangle + \frac{\Delta e}{2} \left(h - e^{(i+1)} \right) \langle \sigma_r^{(i+1)} \rangle \tag{24}$$

Finally, the last approximation makes it possible to determine the average residual stress profile in the $(i+1)^{\text{th}}$ layers as a function of its values taken in the previously machined layer, and of the quantities $(\Sigma_r^j)_{j=\{i,i+1\}}$. Thus

$$\langle \sigma_r^{(i+1)} \rangle = \frac{\Sigma_r^{(i+1)} - \Sigma_r^{(i)} - \frac{\Delta e^2}{2} \sum_{j=1}^{i-1} \langle \sigma_r^{(j)} \rangle}{\Delta e \left(h - e^{(i+1)} \right)}, \forall i \in \{1, ..., n\}. \tag{25}$$

3.5.3 Procedure #2: Retrieving the coefficients governing the polynomial distribution of the residual stress through the thickness of the raw part

The second approach consists in defining the distribution of the residual stress through the thickness of the raw part as a polynomial of degree $2p$, $p \in \mathbb{N}$. Even degrees are chosen here to enforce the symmetry of this distribution with respect to the vertical axis. According to Cherif et al (2019), this distribution is also symmetric with respect to the neutral axis. $(a^{(k)})_{0 \leq k \leq 2p}$ being the coefficients of this polynomial stress distribution denoted by σ_r^p, $\sigma_r^p(y)$ reads

as follows

$$\sigma_r^p(y) = \sum_{k=0}^{p} a^{(k)} \left(\frac{y - \frac{h}{2}}{h} \right)^{2k}. \tag{26}$$

Further simplifications are introduced. Any section of normal $\underline{e}_y$ shall be self-balanced Cheng and Finnie (2007). Thus,

$$i- \int_{y=0}^{h} \sigma_r^p(y) \mathrm{d}y = 0 \quad \text{(force)} \quad \text{and} \quad ii- \int_{y=0}^{h} y\, \sigma_r^p(y) \mathrm{d}y = 0 \quad \text{(force moment)}. \tag{27}$$

The force equilibrium in $i-$ gives the following constraint for the polynomial coefficients:

$$\sum_{k=0}^{p} \frac{a^{(k)}}{2^{2k}(2k+1)} = 0 \tag{28}$$

Concerning $ii-$, the force moment is automatically balanced thanks to the symmetry property of the residual stress distribution.

In the expression of $(\Sigma_r^{(i)})_{1 \leq i \leq n}$ given in Equation 21 above, the stress is then substituted by its simplified version given by the polynomial residual stress defined in Equation 26. After explicitly calculating the integrals involved in this expression, we get the following equation, which is valid for any layer, and in which the $a^{(k)}$ coefficients defining the polynomial function are the unknowns:

$$\begin{aligned} \forall i \in \{1, ..., n\}, \quad \Sigma_r^{(i)} = & \sum_{k=0}^{p} \frac{a^{(k)}}{h^{2k}} \left[\frac{\left(\frac{h}{2}\right)^{2k+2} - \left(\frac{h}{2} - e^{(i)}\right)^{2k+2}}{2k+2} + \cdots \right. \\ & \left. \cdots \frac{e^{(i)}}{2} \frac{\left(\frac{h}{2}\right)^{2k+1} - \left(\frac{h}{2} - e^{(i)}\right)^{2k+1}}{2k+1} \right]. \end{aligned} \tag{29}$$

In practice, the number of machined layers n is much greater than the minimum number of equations needed to determine all the coefficients of the polynomial residual stress σ_r^p, *i.e.* $n \gg p$. For instance, we will have $n =$

86 equations to determine 3 unknown coefficients in the numerical example presented below. The system of equations given in Equation 29 is thus solved by using a classic least squares method.

4 Numerical simulation

4.1 Finite element model

The first step was to check the robustness of this residual stress measurement technique by using synthetic data obtained with a finite element model. The ANSYS 2019 R2 package was used for this purpose. The model was built with the Mechanical "ANSYS Parametric Design Language" (APDL). The initial dimension of the model was $400 \times 100 \times 100\ mm^3$. It is worth remembering that this study is part of a project dealing with issues concerning machining of aeronautical parts. The geometry of the present FE model is assumed to be representative of such parts, which are often slender and not massive.

In the experiment, the workpiece was firmly fixed with two flanges located each at one of its sides. Their load was applied at the bottom of two small notches machined beforehand. These notches were thoroughly reproduced in the FE model, as can be seen in Figure 3 which shows this model after the 86th milling pass, thus at the end of the procedure. The effect of the flanges on the workpiece was modeled by applying a uniform pressure of 52 MPa on the bottom face of the notch, which gives a resulting vertical force of 10 kN. The thin vertical "walls" located at the right- and left-hand sides of the model are caused by the fact that the material is not removed by the tool just above the flange after the 70th pass. These thin walls behave like rigid solids. As such, they do not influence the global deflection of the part.

4.2 Convergence

The constitutive material was assumed to be linear elastic (Young's modulus E=73 GPa, Poisson's ratio $\nu = 0.33$). The model was regularly meshed with 400,000 SOLID185 8-noded elements. Refining further this model by multiplying the number of elements by two along directions x and y, thus by meshing the model with 1.6E+06 elements instead of 0.4E+06, only increases the maximum deflection by 2.1% (from 0.512 mm to 0.523 mm), which is negligible. Thus, we stick with the first mesh for the simulations discussed below.

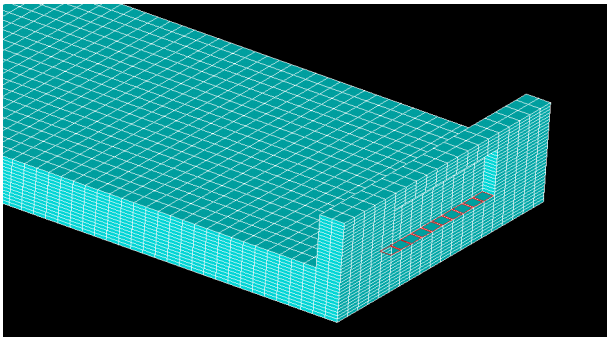

Fig. 3: Perspective view of one of the two lateral sides of the FE model after the 86th pass. The load introduced by the flange was modeled by blocking the nodes located at the bottom of the small notch. This zone is modeled by red lines superposed to the model. The same notch is modeled at the left-hand side of the workpiece.

4.3 Modelling layer removal

An interesting feature of the SOLID185 elements is their ability to account for initial stress distributions entered by the user. In the present case, the polynomial through-thickness distribution of the σ_{xx} discussed in Jovani et al (2022) was considered, with a value only depending on the depth along the thickness. A layer of elements was removed iteratively to model the effect of milling, a new FE calculation being performed for each new value of the thickness. Since

the experiment described below is modeled here and since $n = 86$ successive passes were performed in this experiment, 87 finite element calculations were performed (1 for the initial geometry and 86 for the 86 successive passes), so the thickness iteratively reduced from 100 mm to 15 mm, with a step equal to 1 mm. The strain fields were derived from the nodal displacements collected on the lateral surface of the model after each pass, and these strain maps were considered as synthetic data in the identification procedure described above.

Before presenting the results, it is briefly reminded that in Hospers and Vogelesang (1975), removing a layer is equivalent to saying that the average residual stress through this layer gives rise to a pair of opposite force moments, which are applied to the left- and right-hand sides of the workpiece. The latter is considered as a beam and these force moments are expressed as a function of the curvature of the workpiece. In Hospers and Vogelesang (1975), this average curvature was deduced from the coordinates of three different points. These coordinates were measured by means of a microscope which was attached to a pair of micrometer slides. On the other hand, DIC was used in Jovani et al (2022) to first measure the deflection of the neutral axis and then deduce the average curvature by smoothing and differentiating twice the data, which avoids removing the workpiece from the table of the machine tool between two consecutive passes. This automates and speeds up the procedure. A dedicated integrated DIC version had however to be developed and used to regularize the measurements having regard to the harsh conditions under which the images were taken, while a classic subset-based version of 2D DIC was used in the present study to obtain the strain fields involved in Equation 11.

One might wonder whether in real situations, the deformation of the workpiece could cause the subsequent removed layers to have a thickness different

from the nominal one. The FE simulations performed here show that the deflection between two consecutive passes is equal to 0.006 mm on average, with a maximum value equal to 0.05 mm. These quantities can be considered as negligible compared to the nominal thickness of each removed layer since the latter is equal to 1 mm.

4.4 Representativeness of the measurements performed on the lateral surface

A drawback of the VFM is that it relies on 3D integrals but that the measurements are generally performed on the front face of the specimen only. A common assumption is therefore that the measurements performed on the front face of the specimen are representative of the whole through-thickness displacement field. Since the width of the specimen is not really negligible here compared to its length, we compared the displacement fields provided by the finite element model on the front face of the specimen on the one hand, and its counterpart on the vertical mid-plane on the other hand. This comparison was performed at the very end of the layer removal procedure simulated with the finite element simulations, thus after the 86th pass. The relative difference is depicted in Figure 4. This relative difference is lower than 2.8%, which means that the aforementioned assumption is sound in the present case.

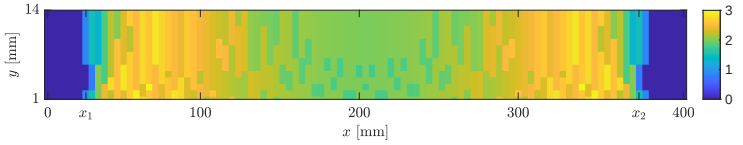

Fig. 4: Relative error between the vertical displacement field estimated by finite element calculation on the front face of the workpiece and its counterpart across the vertical mid-plane, after the 86th pass (in %). The abscissa of the backs of the left- and right-hand notches are denoted by x_1 and x_2, respectively. The scales along x and y are different to more clearly represent the results.

4.5 Comparison between Procedures #1 and #2

The results obtained with synthetic data processed by Procedures #1 and #2 are shown in Figure 5. No noise is added to the data in this case. They are compared with the reference values entered in the finite element model. The value of α, which drives the width of domain $\mathcal{D}_2$ over which W_{int}^* was calculated, was arbitrarily fixed here to $\alpha = 0.3$ (the influence of α on the results is discussed in the following section). This value was chosen to have domain $\mathcal{D}_2$ sufficiently far away from the two supports to avoid any disturbance likely to be caused by the three-dimensional state of stress which takes place in their vicinity. It can be seen that both procedures provide a very similar distribution. Procedure #2 is symmetric by construction, only the even degrees being considered in its expression. Though measurements are only performed for $15 \leq h - e \leq 100$ [mm], the curve obtained with Procedure #2 is plotted for $0 \leq h - e \leq 15$ [mm] in order to observe the difference with the reference curve. The global shape of both curves is similar to the polynomial modeling of the residual stress distribution which was used as input data in the finite element model. The amplitude of the identified residual stress is however lower than the reference one, which is consistent with results presented in Jovani et al (2022) where similar orders of magnitude were found although a different identification technique was used. This is probably due to the fact that the VFM relies on the calculation of 3D integrals (see Equation 4), which all involve stress components, thus real strain components after introducing the constitutive equations. These real strain components are therefore supposed to be available in the bulk, which is not the case in practice. Assuming that we can consider that the strain components in the bulk are equal to their counterparts on the front face of the part, in other words that we deal with a 2D

problem only, certainly causes this difference to appear between identified and reference values.

The relative difference between identified and reference values for the stress peak is equal to 17% with Procedure #1, and to 25 % with Procedure #2 which is significant (this relative difference is slightly lower for the other two peaks). Similar errors were obtained in Jovani et al (2022) although the identification technique used in this reference is completely different. Concerning the influence of α, the results presented in the following section however show that considering higher values for this parameter leads to sharpen the peak with Procedure #2, thus to diminish this error but this increases the random error observed with Procedure #1, which suggests that optimal values for α are different for Procedures #1 and #2. A complete parametric study should be conducted to find the optimal value for each procedure, which is however out of the scope of the present study.

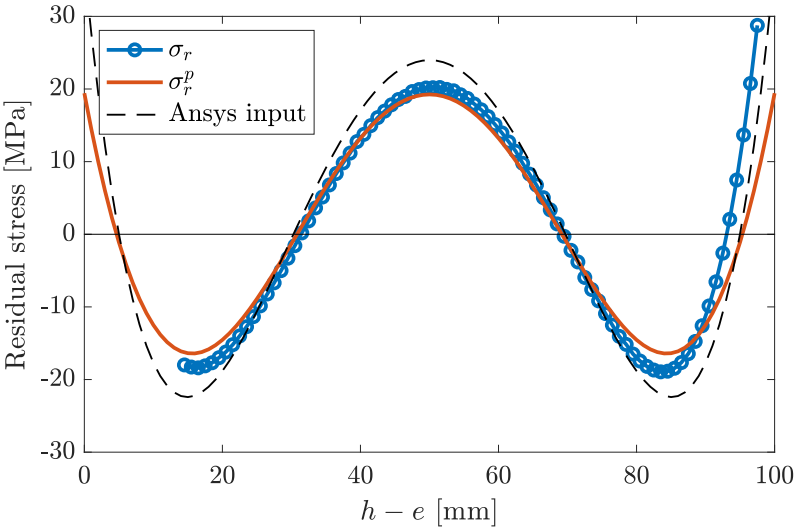

Fig. 5: Residual stress distributions obtained by processing noiseless synthetic data with Procedure #1 (σ_r, calculations performed layerwise) and Procedure #2 (σ_r^p, distribution modeled by a polynomial). $\alpha = 0.3$

4.6 Influence of α

The influence of α on the results is investigated here. Its value increases from 0 to 0.4 with a step of 0.04, which means that the zone considered to perform the calculation (see $\mathcal{D}_2$ in Figure 2) progressively decreases. Figure 6 shows various residual stress distributions obtained with Procedures #1 and #2 when increasing the value of α.

Two main remarks can be drawn from these results. First, the global aspect of the though-thickness stress field remains unchanged as α increases, which means that no significant model error occurs near the support of the workpiece, where it is still assumed that the measurement performed over the lateral surface is equal to its value in the bulk. However, the actual stress field is certainly tridimensional because of the clamps. The curves become more and more affected by random fluctuations as α increases. This is logical since domain $\mathcal{D}_2$ considered to calculate W_{int}^* (see Equation 11), thus the residual stress estimation, reduces as α increases. This causes the influence of noise to be more and more visible.

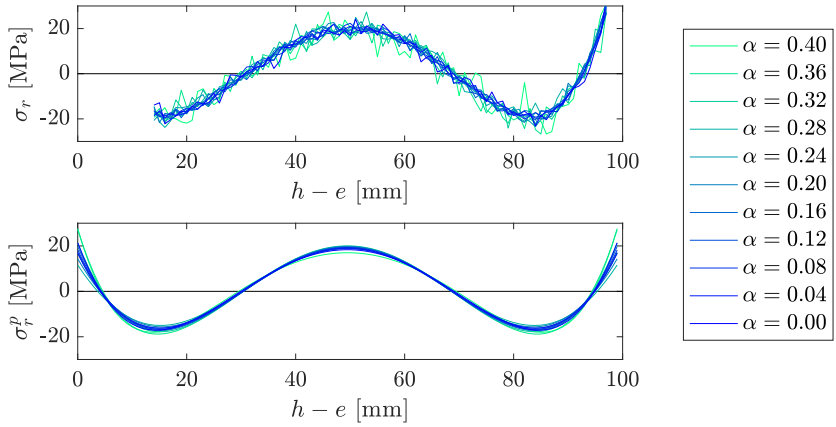

Fig. 6: Influence of α on the results. Top: Procedure #1. Bottom: Procedure #2.

This result can be quantified by plotting in Figure 7 the difference between the standard deviation of the difference between the estimations of the residual stress distributions for various values of α for both procedures on the one hand, and the residual stress distribution obtained with σ_r^p and $\alpha = 0$ on the other hand. This last choice is somewhat arbitrary but this helps to visualize the influence of this parameter.

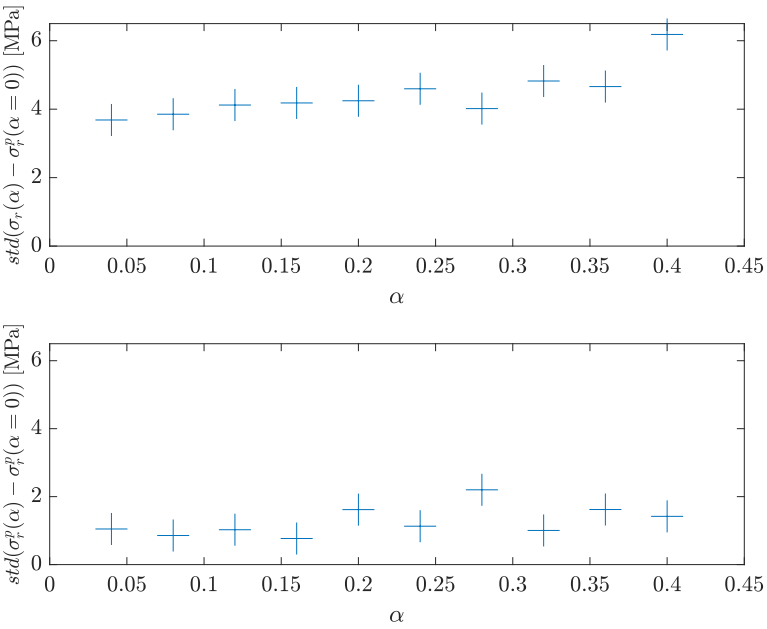

Fig. 7: Influence of α on the results. Top: Procedure #1. Bottom: Procedure #2.

4.7 Sensitivity to noise of Procedures #1 and #2

A white Gaussian noise of standard deviation std_u was also added to the nodal displacements provided by the finite element calculation in order to assess the robustness of the procedure. The models of noise affecting real displacement maps are generally more complicated Sutton et al (2009) but employing a

mere Gaussian noise is a common means to assess the robustness of procedures which identify parameters from displacement or strain maps, Avril et al (2004) for instance. This is therefore the method which was used here. Four different values of std_u were considered: namely $std_u = 10^{-4}$, 10^{-3}, 10^{-2} and 10^{-1} [px]. $10^{-3}/10^{-2}$ pixel is the order of magnitude of the displacement resolution generally obtained with DIC used in the context material characterization Sutton et al (2009). In the present case however, this displacement resolution is certainly worst (thus higher) because of the conditions under which DIC was applied Rebergue et al (2018, 2022), which justifies the fact that the case of 10^{-1} [px] was also considered in this simulation.

Typical noisy trough-thickness residual stress distributions are shown in Figure 8. It can be seen that the results are much more affected by noise with Procedure #1 (σ_r) than with Procedure #2 (σ_r^p), with significant fluctuations for $std_u = 10^{-1}$ [px]. This is logical since the identification procedure provides only 3 coefficients governing the fourth-degree polynomial (with only even degrees) from the 86 equations given by the PVW written layerwise. On the other hand, 86 discrete values are obtained from 86 equations by using Procedure #1.

100 copies of the same noise were then randomly generated with the randn function of Matlab© for each value of std_u, so 100 residual stress distributions were obtained for each procedure and for each of the four values of std_u. For Procedure #1, the standard deviation $std^{(\sigma_r(y_i))}$ of the fluctuating value of the residual stress $\sigma_r(y_i)$ was estimated for each value of $std^{(u)}$. A global estimation of the noise affecting the results was deduced by considering the global standard deviation std_g of the noise affecting the residual stress through the thickness, with

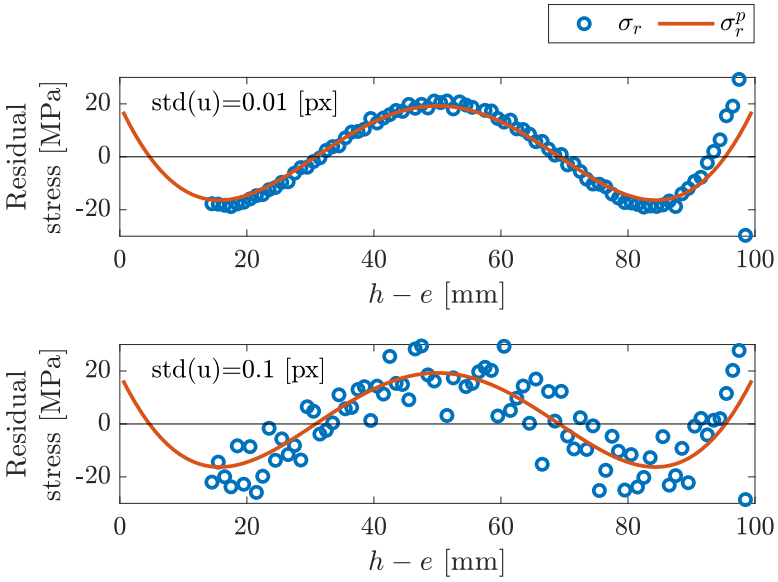

Fig. 8: Stress distributions obtained with noisy data in two cases: std_u=0.01 [px] (top) and std_u=0.1 [px] (bottom).

$$std_g = \sqrt{\sum_{i=1}^{n} \frac{\left(std^{(\sigma_r(y_i))}\right)^2}{n}} \tag{30}$$

where n is the number of layers, hence $n = 86$. The same quantity was considered for Procedure #2 by substituting $\sigma_r(y_i)$ by $\sigma_r^p(y_i)$ in this equation in order to keep the same number of though-thickness measuring points for both procedures, which makes the results comparable from one procedure to another. Figure 9 gives std_g as a function of std_u

The visual aspect of the results given in Figure 8 is quantified here, with more than one order of magnitude between the values of std_g obtained with Procedures #1 and #2. The global error std_g remains acceptable with the highest values of std_u, but with Procedures #2 only, which means that the present identification procedure can actually be used in these adverse experimental conditions.

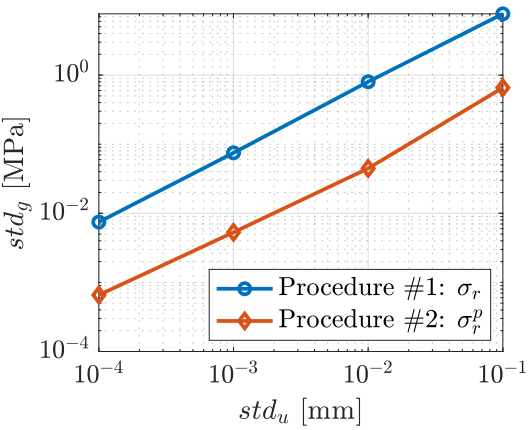

Fig. 9: std_g vs. std_u for Procedures #1 and #2.

5 Experimental results

We consider now the set of experimental data obtained in Rebergue et al (2022) and processed in Jovani et al (2022). These data were obtained by equipping a 5-axe CRENO high-speed machine tool with a 5-DSR Canon camera. A TAMRON 90 mm F2.8 Di MACRO 1:1 VC USD lens was mounted on this camera. This camera was directly fixed on the machine table with a dedicated support. The lighting system was also directly mounted on the table. The experimental setup is shown in Figure 10.

The workpiece under study was cut in an Al7010-T7451 aluminum alloy sheet metal obtained by lamination. The dimensions are the same as those of the model discussed in the preceding section. $n = 86$ successive milling passes were performed with a Sandwick R590-110504H-NL H10 D100 milling cutter equipped with six Sandwick R590-110504H-NL H10 inserts. The cutting speed was equal to 1000 m/mn, the depth of cut to 1 mm and the spindle speed to 3183 rounds/mn. More details on this experimental setup and on the cutting parameters used during machining are available in Rebergue et al (2022);

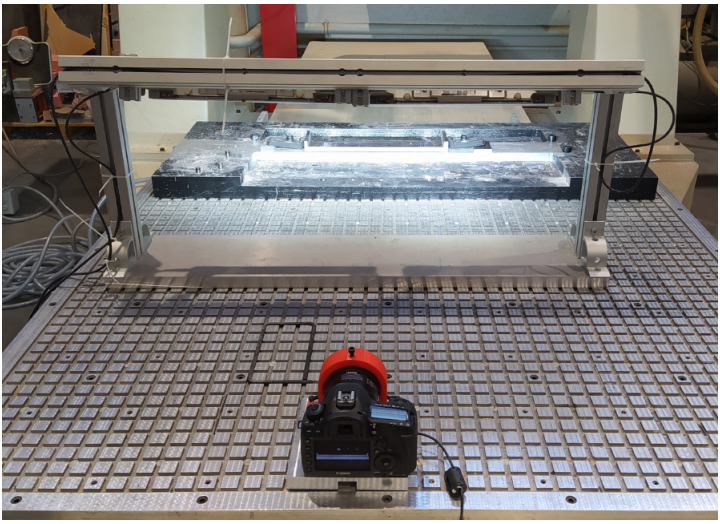

Fig. 10: Experimental setup, after Rebergue et al (2022); Jovani et al (2022).

Jovani et al (2022). It is worth emphasizing that the present working conditions are worse compared to what happens with the classic use of a DIC system for the purpose of material characterization. In this latter case, a DIC system is typically placed in front of a testing machine, and the camera takes pictures of the specimen which gently deforms. In the present case, the table on which the camera was fixed was allowed to move at high-speed (this is one of the axes of the machine tool), and the device which supports the spindle and tool also moved at high-speed. These movements unavoidably caused vibrations to occur, and the amplitude of these vibrations was significant compared to the tiny displacements caused by the deformation of the workpiece during milling, not to mention the fluctuating lighting and the metal cutting chips flying around. DIC was therefore tailored for this purpose in Rebergue et al (2022); Jovani et al (2022). In these references, it is for instance explained how the rigid-body motion caused by vibrations was deduced from the apparent displacement of the workpiece measured by DIC, by subtracting the movement of the support placed beneath the workpiece, which was also measured

Subset size	51×51 pixels^2
Shift	25 pixels
Shape function	affine
Interpolation function	bicubic polynomial
Correlation criterion	Sum of Squared Difference
Pre-smoothing applied to the images	none
Camera	8 bits, 8688×3401 pixels
Fields of view	164×419 mm
Differentiation method	central difference
Smooting method	no smoothing

Table 1: Experimental DIC settings and performances (according to International Digital Image Correlation Society, Jones, E.M.C. and Iadicola, M.A. (Eds) (2018))

by DIC. In the present study, a classic local DIC in-house-developed program was used to obtain the strain fields involved in the PVW. The parasitic displacement caused by the vibrations of the table was also subtracted by using the procedure described in Rebergue et al (2022). The DIC parameters (as defined in International Digital Image Correlation Society, Jones, E.M.C. and Iadicola, M.A. (Eds) (2018)) are reported in Table 1. The actual displacement and strain being expected to be smooth over $\mathcal{D}_2$, the subset size was quite large to diminish the effect of noise. A typical u_x displacement map along with the corresponding ε_{xx} strain map are depicted in Figure 11. It can be seen in Figure 11a that the displacement gently changes over the lateral surface, without strong apparent gradients. The corresponding ε_{xx} strain map in Figure 11b illustrates that DIC is in this case at the limits of what can be measured with this technique in such an environment, which noise and a small strain amplitude, and that only global quantities such a those obtained with VFM by weighted averaging the latter strain map can eventually provide relevant information.

The residual stress distributions obtained with Procedures #1 and #2 are reported in Figure 12, along with the results provided by the method described in Jovani et al (2022) for comparison purposes. As already mentioned above

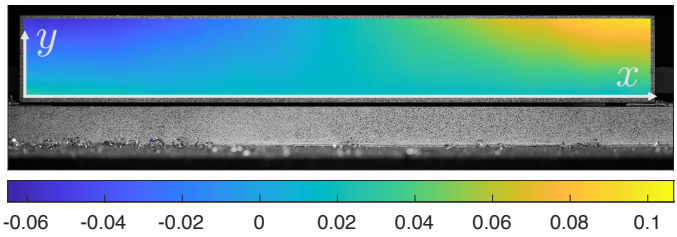

(a) u_x

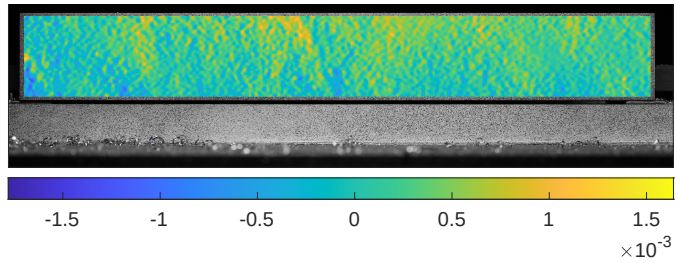

(b) ϵ_{xx}

Fig. 11: Typical u_x displacement map and ϵ_{xx} strain map obtained during milling after the 45th pass.

for the simulated data, the results obtained with Procedure #1 are much noisier than their counterparts obtained with Procedure #2. Interestingly, the scatter of the results decreases as the thickness of the part h decreases, thus as the number of passes increases. This is due to the fact that the number of experimental data progressively increases, which progressively reduces the influence of noise. The experimental results obtained with Procedure #1 are also noisier than those given by the procedure developed in Jovani et al (2022). This is due to the fact that a dedicated integrated DIC program was developed in Jovani et al (2022) by accounting for the fact that the part deformed like a beam. The classic kinematic assumption linking curvature and through-thickness displacement was therefore considered in this reference. On the other hand, a standard subset-based DIC program was used with Procedure #1 to obtain the experimental data, without any a priori assumption on the nature

of the through-thickness displacement, apart from the fact that it is bidimensional and locally modeled by the shape function of the subsets. Comparing the curve provided by Procedure #2 and the curve obtained by fitting with an even fourth-degree polynomial the experimental points given by the procedure developed in Jovani et al (2022) shows that the obtained results are very similar although the strategies employed to obtain them are completely different. From these results, it can be concluded that compared to the procedure developed in Jovani et al (2022), the benefit of using the approach proposed here which relies on the VFM is twofold:

- A standard subset-based DIC program has been employed here to measure the displacement field, while an integrated version had to be specifically developed in Jovani et al (2022);
- Contrary to the procedure proposed in Jovani et al (2022), no assumption concerning the through-thickness strain/stress distributions is used, which means that the present approach is more general and could potentially be applied to more complicated workpiece geometries.

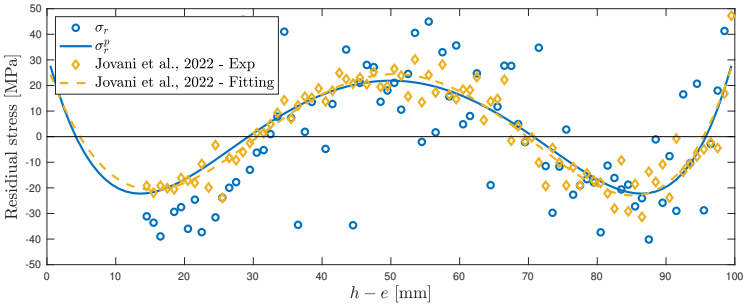

Fig. 12: Estimation of the residual stress obtained with different approaches as a function of the current thickness $h-e$ of the remaining part of the workpiece: σ_r with Procedure #1, σ_r^p with Procedure #2 and the method given in Jovani et al (2022) before and after polynomial fitting. Experimental data are only available for $h-e \geq 15$ mm.

6 Conclusion

The measurement of the residual stress distribution during machining of a slender workpiece was addressed in this paper. DIC was used to measure the displacement field after each pass. The resulting strain fields were then used as input data in the Virtual Fields Method to deduce the through-thickness distribution of the residual stress. The first conclusion is that a classic subset-based version of DIC can be used to measure the displacement field on the lateral surface of the workpiece despite the harsh environment under which the experiment is performed (vibrations, cutting chips flying around, fluctuating lighting of the zone of interest). Another conclusion is that no assumption is made about the through-thickness displacement field in the workpiece with this approach based on the VFM, which paves the way for future applications dealing with more complex geometries or machining sequences, provided that the side face over which full-field measurements are performed remains unobstructed and that the aspect ratio of the workpiece is high enough for considering the in-plane stress assumption as acceptable. More complex virtual fields suited to the problem at hand should also certainly be defined.

Acknowledgements

This work has been sponsored by the French government research program "Investissements d'Avenir" through the IDEX-ISITE initiative 16-IDEX-0001 (CAP 20-25). The authors also gratefully acknowledge the financial supports from the French National Research Agency (ANR) through the ICAReS and IMaDe projects (ANR-18-CE08-0028-01 and ANR-19-CE10-0002 grants, respectively), and from the AURA regional council.

Ethics declarations/Conflict of Interest

The authors declare that they have no conflict of interest.

References

ASTM (2021) ASTM E 837 : Standard test method for determining residual stress by the hole drilling strain-gauge method. URL https://www.astm.org/standards/e837, ASTM Standard, American Society for Testing and Materials

Avril S, Grédiac M, Pierron F (2004) Sensitivity of the virtual fields method to noisy data. Computational Mechanics 34:439–452

Baldi A (2014) Residual stress measurement using hole drilling and integrated digital image correlation techniques. Experimental Mechanics 54(3):379–391

Baldi A (2019) On the implementation of the integral method for residual stress measurement by integrated digital image correlation. Experimental Mechanics 59(7):1007–1020

Berry A, Olivier R (2016) Identification of spatially correlated excitations on a bending plate using the Virtual Fields Method. Journal of Sound and Vibration 375:76–91

Berry A, Robin O, Pierron F (2014) Identification of dynamic loading on a bending plate using the Virtual Fields Method. Journal of Sound and Vibration 333(26):7151–7164

Billur E (2020) Digital image correlation: How it changed the bulge test. Metal Forming Magazine pp 978–985

Cao Q, Li Y, Xie H (2020) Orientation-identified Virtual Fields Method combined with moiré interferometry for mechanical characterization of single crystal Ni-based superalloys. Optics and Lasers in Engineering 125:105,854

Cheng W, Finnie I (2007) Residual stress measurement and the slitting method. Springer Science & Business Media, https://doi.org/https://doi.org/10.1007/978-0-387-39030-7

Cherif I, Cotton D, Poulachon G, et al (2019) Instrumented clamping device and numerical simulations to study machining distortion. The International Journal of Advanced Manufacturing Technology 105(7):3093–3103

Corigliano P, Crupi V, Pei X, et al (2021) DIC-based structural strain approach for low-cycle fatigue assessment of aa 5083 welded joints. Theoretical and Applied Fracture Mechanics 116:103,090

Dreier S, Denkena B (2014) Determination of residual stresses in plate material by layer removal with machine-integrated measurement. Procedia CIRP 24:103–107

Dym J, Shames H (1973) Solid Mechanics: A Variational Approach. McGraw-Hill Book Company, New York, 685 pages, ISBN: 978-0070185562

Gao J, Shang H (2009) Deformation pattern based digital image correlation method and its application to residual stress measurement. Applied Optics 48(7):1371–1381

Grédiac M (1989) Principe des travaux virtuels et identification. Comptes Rendus de l'Académie des Sciences 309-II:1–5. Gauthier-Villars. In French with abridged English version.

Grédiac M, Hild F (eds) (2012) Full-field measurements and identification in solid mechanics. Wiley, iSBN: 9781848212947, 496 pages

Grédiac M, Sur F, Blaysat B (2016) The grid method for in-plane displacement and strain measurement: a review and analysis. Strain 52(3):205–243

Harzallah M, Pottier T, Gilblas R, et al (2018) A coupled in-situ measurement of temperature and kinematic fields in ti-6al-4v serrated chip formation at micro-scale. International Journal of Machine Tools and Manufacture 130-131:20–35

Hospers F, Vogelesang L (1975) Determination of residual stresses in aluminum-alloy sheet material. Experimental Mechanics 15(3):107–110

International Digital Image Correlation Society, Jones, E.M.C. and Iadicola, M.A. (Eds) (2018) A good practices guide for Digital Image Correlation. https://doi.org/10.32720/idics/gpg.ed1, online

Jiang LM, Peng J, Liao YG, et al (2011) A modified layer-removal method for residual stress measurement in electrodeposited nickel films. Thin Solid Films 519(10):3249–3253

Jovani T, Chanal H, Blaysat B, et al (2022) Direct residual stress identification during machining. Journal of Manufacturing Processes https://doi.org/https://doi.org/10.1016/j.jmapro.2022.08.015, accepted, online

Kaufmann R, Ganapathisubramani B, Pierron F (2019) Full-field surface pressure reconstruction using the Virtual Fields Method. Experimental Mechanics 59(8):1203–1221

Kaufmann R, Olufsen S, Fagerholt E, et al (2022) Reconstruction of surface pressures on flat plates impacted by blast waves using the virtual fields method. International Journal of Impact Engineering p 104369

Louëdec GL, Pierron F, Sutton M, et al (2013) Identification of the local elasto-plastic behavior of FSW welds using the Virtual Fields Method. Experimental Mechanics 53(5):849–859

Martins J, Andrade-Campos A, Thuillier S (2018) Comparison of inverse identification strategies for constitutive mechanical models using full-field measurements. International Journal of Mechanical Sciences 145:330–345

Milosevic N, Younise B, Sedmak A, et al (2021) Evaluation of true stress–strain diagrams for welded joints by application of digital image correlation. Engineering Failure Analysis 128:105,609

Mishra A, Thuillier S (2014) Investigation of the rupture in tension and bending of DP980 steel sheet. International Journal of Mechanical Sciences 84:171–181

O'Donoughue P, Robin O, Berry A (2019) Time-space identification of mechanical impacts and distributed random excitations on plates and membranes. Proceedings of the Institution of Mechanical Engineers, Part C: Journal of Mechanical Engineering Science 233(18):6436–6447

Olson MD, Watanabe BT, Wong TA, et al (2022) Near surface residual stress measurement using slotting. Experimental Mechanics Accepted, online

Olufsen SN, Kaufmann R, E.Fagerholt, et al (2022) RECOLO: A Python package for the reconstruction of surface pressure loads from kinematic fields using the Virtual Fields Method. Journal of Open Source Software 7(71):3980

Pierron F, Grédiac M (2012) The Virtual Fields Method. Springer, 517 pages, ISBN: 978-1-4614-1823-8

Pierron F, Grédiac M (2021) Towards Material Testing 2.0. A review of test design for identification of constitutive parameters from full-field measurements. Strain 57(1):e12,370

Pierron F, M.A., Sutton, et al (2011) Ultra high speed DIC and Virtual Fields Method analysis of a three-point bending impact test on an aluminium bar. Experimental Mechanics 51(4):537–563

Pottier T, Vacher P, Toussaint F, et al (2012) Out-of-plane testing procedure for inverse identification purpose: Application in sheet metal plasticity. Experimental Mechanics 52(7):951–963

Prime MB, Hill MR (2002) Residual stress, stress relief, and inhomogeneity in aluminum plate. Scripta Materialia 46(1):77–82

Razumovskii IA, Usov SM (2021) Development of the hole-drilling method as applied to the study of inhomogeneous residual stress fields. Journal of Machinery Manufacture and Reliability 50(8):727–734

Rebergue G, Blaysat B, Chanal H, et al (2018) Advanced DIC for accurate part deflection measurement in a machining environment. Journal of Manufacturing Processes 33:10–23

Rebergue G, Blaysat B, Chanal H, et al (2022) In-situ measurement of machining part deflection with digital image correlation. Measurement 187:110,301

Salehi SD, Rastak MA, Shokrieh MM, et al (2020) Full-field measurement of residual stresses in composite materials using the incremental slitting and digital image correlation techniques. Experimental Mechanics 60(9):1239–1250

Schwindt CD, Stout M, Iurman L, et al (2015) Forming limit curve determination of a dp-780 steel sheet. Procedia Materials Science 8:978–985

Sutton M, Orteu J, Schreier H (2009) Image Correlation for Shape, Motion and Deformation Measurements. Basic Concepts,Theory and Applications. Springer

Texier D, Zedan Y, Amoros T, et al (2016) Near-surface mechanical heterogeneities in a dissimilar aluminum alloys friction stir welded joint. Materials & Design 108:217–229

Treuting RG, Read WT (1951) A mechanical determination of biaxial residual stress in sheet materials. Journal of Applied Physics 22:130–134

Zhang L, Thakku S, Beotra M, et al (2017) Verification of a Virtual Fields Method to extract the mechanical properties of human optic nerve head tissues in vivo. Biomechanics and Modeling in Mechanobiology 16(3):871–887